RSC Advances

PAPER

View Article Online
View Journal | View Issue

Cite this: *RSC Adv.*, 2020, **10**, 32569

The mechanism for CO_2 reduction over Fe-modified Cu(100) surfaces with thermodynamics and kinetics: a DFT study†

Mei Qiu, *[ab] Yi Li [c] and Yongfan Zhang [c]

The adsorption, activation and reduction of CO_2 over Fe_x/Cu(100) (x = 1–9) surfaces were examined by density functional theory. The most stable structure of CO_2 adsorption on the Fe_x/Cu(100) surface was realized. The electronic structure analysis showed that the doped Fe improved the adsorption, activation and reduction of CO_2 on the pure Cu(100) surface. From the perspective of thermodynamics and kinetics, the Fe_4/Cu(100) surface acted as a potential catalyst to decompose CO_2 into CO with a barrier of 32.8 kJ mol^{-1}. Meanwhile, the first principle molecular dynamics (FPMD) analysis indicated that the decomposition of the C–O1 bond of CO_2 on the Fe_4/Cu(100) surface was only observed from 350 K to 450 K under a CO_2 partial pressure from 0 atm to 10 atm. Furthermore, the results of FPMD analysis revealed that CO_2 would rather decompose than hydrogenate when CO_2 and H co-adsorbed on the Fe_4/Cu(100) surface.

Received 20th July 2020
Accepted 24th August 2020

DOI: 10.1039/d0ra06319c

rsc.li/rsc-advances

1. Introduction

Reducing the concentration of CO_2 in the atmosphere has attracted significant attention, because as the major component of greenhouse gas, excessive emissions of CO_2 have contributed significantly to environment degradation in the past decades, such as global warming, and melting of glaciers. The conversion of CO_2 as a C resource to synthesize more valuable chemical raw materials not only solves the major crisis of global greenhouse gases and energy shortage, but also provides great opportunities and challenges for exploring novel catalysts and developing a modern catalytic industry.[1]

Because CO_2 is a thermodynamically stable molecule, it is difficult to utilize CO_2 as the C resource.[2] Currently, five ways to reduce CO_2 have been reported: (i) electrocatalytic reduction,[3–8] (ii) photocatalytic reduction,[2,9–11] (iii) thermal catalytic reduction,[12–15] (iv) enzymatic reduction[16,17] and (v) photo-electrocatalytic reduction.[18] In these cases, the catalyst plays a major role in CO_2 activity and reduction.

Numerous experiments and theories have been used to investigate the adsorption, activation and reduction of CO_2 on transition metal–based catalysts.[19–27] For instance, Fierro systematically investigated the adsorption of CO_2 on the Co(100), Co(110) and Co(111) surfaces.[19] The results indicated that the adsorption configuration of CO_2 on the substrate was sensitive, especially the Co(110) surface. The experimental results of Rasmussen showed that the Cu(100) surface was able to decompose CO_2 into CO and O_2.[22] Roberts demonstrated that CO_2 could be decomposed into CO on the Ni(100) surface rather than on the Ni(111) surface.[23] Ding asserted that a weak interaction was formed between CO_2 and the Ni(110) surface.[24] Glezakou investigated the mechanism of adsorption and activation of CO_2 on the Fe fcc(100) surface.[25] Their results indicated that CO_2 on the Fe(100) surface was activated spontaneously. Wilson investigated the reduction of CO_2 into CO on Co(100), Ni(100) and Cu(100) surfaces.[26] The calculated results revealed an interesting trend between reaction energy and the total reaction barrier from Fe to Cu and that reactions tended to be less exergonic. Additionally, Co and Ni were more favorable to decompose CO_2 into CO.

Except for the single metal catalysts for CO_2, Great effort has been devoted to improve the catalytic performance of bimetallic catalysts for CO_2 activation and catalysis.[27,28] Nerlov pointed out that the performance of Cu–Ni bimetallic catalyst was more than 60 times greater than the pure Cu.[29–31] Liu found that the introduction of Pd, Rh, Pt, and Ni metals on the Cu(111) surface promoted the methanol production.[32] Our previous reports revealed that the introduction of a second metal could improve the interaction between CO_2 and the Cu(100) surface.[33,34] Additionally, the results also showed that the interaction between CO_2 and the Co_n/Cu(100) surface was structure sensitive for the reduction of CO_2 molecules and the Co_4/Cu(100) surface was the potential catalyst for the reduction of CO_2. The

[a]*Department of Chemistry, College of Science, Jiangxi Agricultural University, Nanchang, Jiangxi, 330045, China. E-mail: qium@jxau.edu.cn*

[b]*State Key Laboratory of Structural Chemistry, Fujian Institute of Research on the Structure of Matter, Chinese Academy of Sciences, 350002 Fuzhou, Fujian, 350002, China*

[c]*College of Chemistry, Fuzhou University, Fuzhou, Fujian, 350116, China*

† Electronic supplementary information (ESI) available. See DOI: 10.1039/d0ra06319c

results of Song demonstrated that the properties of CO_2 conversion on Fe–Ni and Fe–Co catalysts were similar, and CO* and HCOO* were the preferred intermediates.[35,36]

On the basis of these reports, in this work the density functional theory calculations was employed to understand the activation and reduction of CO_2 on the Cu(100) surface with embedded small Fe atoms. The result of a recent STM experiment showed that small Co clusters can be formed in the first layer of the Cu(100) surface through the vacancy-mediated diffusion of Co atoms.[37] The similarity of the Co/Cu(100) and Fe/Cu(100) epitaxial systems suggests that the diffusion of embedded Fe atoms also leads to the formation of small nanostructures.[38] Firstly, the most stable structure of Fe_x/Cu(100) (x = 1–9) was generated using the first principle molecular dynamics (FPMD) method. Then the adsorption energetics and geometry, vibrational frequencies analysis, charge transfers and d-band center of CO_2 over a series of Fe_x/Cu bimetallic surfaces were analyzed. The activation energy barrier for the CO_2 reduction and the Brønsted–Evans–Polanyi (BEP) relationships between the kinetic parameters for CO_2 reduction over the Fe_x/Cu(100) systems were investigated. And then the optimal temperature and partial pressure for CO_2 reduction on the Fe_4/Cu(100) surface was explored in detail. Lastly, the hydrogenation of CO_2 and residual CO or O was considered in the paper.

2. Computation details

2.1. Method

All of the density functional theory (DFT) calculations using the Vienna *ab initio* simulation package (VASP)[39–41] were according to projector-augmented wave DFT (PAW-DFT).[42–44] The Perdew–Burke–Ernzerhof (PBE) functional based on the generalized gradient approximation was employed.[45] The kinetic energy cutoff of 400 eV for the plane-wave expansion was set. In all systems, the effects of dipole correction, spin polarization in the surface normal direction and the van der Waals correction were considered by using DFT-D2 method.[46,47] Geometrical structure was optimized until the energy change and the maximum force were less than 10^{-6} eV and 0.02 eV Å^{-1}, respectively. The 5 × 5 × 1 k-points with Monkhorst–Pack method were used.[48]

2.2. Surface model

Previous studies reveal that the Cu(100) surface is the most potential value to be reduction of CO_2 molecule among Cu(100), Cu(110) and Cu(111) surfaces.[34] Thus, the Cu(100) surface with a $p(3 \times 3)$ supercell and five atomic layers was employed. For the Fe_x/Cu(100) (x = 1–9) surfaces, Cu atoms on top-layer of the pure Cu(100) surface were substituted by several Fe atoms. In the geometry optimizations, the top three layers were completely relaxed in all directions and the bottom two layers were fixed in their bulk position. The vacuum of 15 Å between the adjacent slabs was set along the c-axis direction to avoid periodic interactions.

The adsorption energy (E_{ads}) for the CO_2 molecule on the Fe_x/Cu(100) surface was defined eqn (1), as follows:

$$E_{ads} = E_{CO_2} + E_{Slab} - E_{CO_2/Slab} \quad (1)$$

where, E_{CO_2}, E_{Slab} and $E_{CO_2/Slab}$ represent the total energy of the free CO_2 molecule in the gas phase, the clean surface and the slab with adsorbed CO_2, respectively. Therefore, a negative value of E_{ads} indicates an endothermic adsorption and a positive value refers to an exothermic adsorption.

The reduction of CO_2 on the Fe_x/Cu(100) surface was involved in the formations of CO and HCOO, namely, $CO_2(g) \rightarrow CO_2^* \rightarrow CO^* + O^*$ and $CO_2^* \rightarrow H^* + HCOO^*$ (where X* represents X species adsorbed on substrate). The corresponding activation energy barrier was calculated from the relative energy of the transition state (TS) with respect to the sum of the energies of the initial structure (IS) (CO_2 adsorbed on the Fe_x/Cu(100) surface), namely,

$$E_a = E_{TS} - E_{IS} \quad (2)$$

All the transition states were determined using the climbing image nudged elastic band (CI-NEB)[49,50] and DIMER[51,52] methods and performed a vibrational frequency analysis to confirm that the predicted transition state to the first-order saddle point in the reaction path. Additionally, the Bader charge analysis using the code developed by Henkelman and coworkers was employed to quantify the charge transfer between the substrates and CO_2 molecule.[53–55]

2.3. Microkinetic model

The rate constants for CO_2 dissociation using the harmonic transition state theory[56–58] was analyzed as shown in eqn (3):

$$k = A \exp\left(-\frac{E_{act}}{RT}\right) \quad (3)$$

where, A represents the pre-exponential factor. According to the harmonic transition state theory, the pre-exponential factor (A) can be estimated using the following formula:

$$A = \frac{\prod_{i-1}^{3N} f_i^{IS}}{\prod_{i-1}^{3N-1} f_i^{TS}} \quad (4)$$

where f_i^{IS} and f_i^{TS} were the vibrational frequencies at the IS and the TS. Note that the imaginary frequency in TS was excluded.

The actual activation barrier (E_{act}), including the entropy (ΔTS), the zero point energy (ZPE) and enthalpy ($\int C_p dT$) corrections, was calculated as follows:

$$E_{act} = E_a + \Delta ZPE - \Delta TS + \Delta \int C_p dT \quad (5)$$

where, S and C_p represent the entropy and the heat capacity, respectively. The zero point energy, entropy and enthalpy correction are calculated as follows,[57] respectively:

$$ZPE = \frac{1}{2}\sum_i hf_i \quad (6)$$

$$-TS = k_b T \sum_i \ln\left(1 - e^{-\frac{hf_i}{k_b T}}\right) - \sum_i hf_i \left(\frac{1}{e^{\frac{hf_i}{k_b T}}} - 1\right) - k_b T \quad (7)$$

$$\int C_p dT = \sum_i hf_i \left(\frac{1}{e^{-\frac{hf_i}{k_b T}} - 1} \right) + k_b T \quad (8)$$

where f_i was the vibrational frequency and i represents the different modes of vibration.

To calculate the relative concentrate (θ_{CO}) of CO on the Fe–Cu bimetallic system, the steady state approximation was adopted in this work.[59] The total amount of metal catalytic sites in the reaction was considered as a constant and the sum of the occupied (θ_x) and the free metal (θ_*) sites were defined as following eqn (9):[60]

$$\theta_{CO_2} + 2\theta_{CO} + \theta_* = 1 \quad (9)$$

where θ_{CO_2} was obtained by $\theta_{CO_2} \times K_{CO_2} \times P_{CO_2} \times \theta_*$ and $K_{CO_2} = \exp\left(-\frac{E_{ads} - T\Delta S}{RT} \right)$.[61] The partial pressure (P_{CO_2}) of CO_2 from 0 to 10 atm was set.

For the elementary reaction step $CO_2 \rightarrow^{k_+}_{k_-} CO + O$ (rate constants, $K = \frac{k_+}{k_-}$), according to the steady-state approximation, the equation was as follows:

$$\frac{dCO}{dt} k_+ \theta_{CO_2} - k_- \theta_{CO} = 0 \quad (10)$$

Thus,

$$\theta_{CO} = \frac{1}{2 + 1/K + 1/(K \times K_{CO_2} \times P_{CO_2})} \quad (11)$$

3. Results and discussion

The most stable structure of the different coverage (n) for Fe dopant on the top-layer of the Cu(100) surface was discussed briefly.

If $n > 1/9$ ML, more than one possible structure of Fe could be doped in the Cu(100) surface. Optimal doping structure for the different coverage of Fe dopant was predicted after extensive study of the various arrangements of Fe atoms embedded in the top-layer of the Cu(100) surface. Taking Fe_4/Cu(100) as an example, four possible configurations for the Fe_4/Cu(100) surface, namely: M1 ~ M4, (see Fig. 1), were considered. In the M1 model, four Fe atoms tended to gather together and form a square nanocluster. For the M2 and M3 structure, the four Fe atoms exhibited the T- and Z-type structure, respectively. In the M4 structure, it was seen as the Fe_3 trimer and an isolated Fe atom. The calculated relative energies (Fig. 1) indicated that the energetically most favorable configuration among the M1 ~ M4 models was the M1. The most stable structure for the Fe_x/Cu(100) surfaces was determined by the similar approach and shown in Fig. S1.† Interestingly, from the perspective of thermodynamic, Fe dopant tended to arrange together when the n values increased from 1/9 to 1 ML. Therefore, we focused on the adsorption, activation and reduction of CO_2 molecule on the most stable configuration for the Fe_x/Cu(100) surfaces.

3.1. Adsorption configurations of CO_2 on Fe_x/Cu(100) surfaces

The most stable structure of CO_2 on the Fe_x/Cu(100) (x = 1–9) surface was presented in Fig. 2, including CO_2 on the pure Cu(100) and Fe fcc(100) surfaces. It was clearly observed in Fig. 2 that the adsorption behavior of CO_2 on the Fe_x/Cu(100) surface was sensitive to the coverage of Fe atoms when the coverage of Fe atoms was less than 4/9 ML (Fig. 2(a)–(c)). While the coverage was more than 4/9 ML (Fig. 2(d)), the adsorption configuration of CO_2 on the Fe_x/Cu(100) surface (Fig. 2(e)–(i)) was similar to the structure of CO_2 on the Fe_4/Cu(100) surface. Herein, it was worth noting that the O atoms in the CO_2 molecule tended to bind with the Fe atoms on the substrate *via* forming Fe–O adsorption bonds because the strength of the Fe–O bond was stronger than the Cu–O bond (*e.g.*, in a diatomic molecule, the dissociation energies of the Fe–O bond and Cu–O bond were about 390.4 and 269.0 kJ mol^{-1}, respectively), indicating that the introduced Fe atoms were the major center of CO_2 adsorption and activation.

After CO_2 adsorption, some electrons were transferred from the substrate to CO_2 moiety, leading to the bent structure with the O–C–O bond angle from 118° to 135° (Table 1). Furthermore, the C–O1 bond and the C–O2 bond was stretched to about 1.253 to 1.364 Å and 1.253 to 1.300 Å, respectively. Especially the C–O1 bond, its distance was gradually elongated by 0.2 Å compared with the distance of 1.176 Å in gas-phase CO_2 molecule when the coverage of the Fe atoms was more than 3/9 ML, which meant that the C–O1 bond was activated after CO_2 adsorption. Meanwhile, it was also noticed that when the coverage of the Fe atoms was more than 3/9 ML, the extra interaction between the O2 atom in the CO_2 moiety and the Fe atom was established and the corresponding Fe–O2 bond

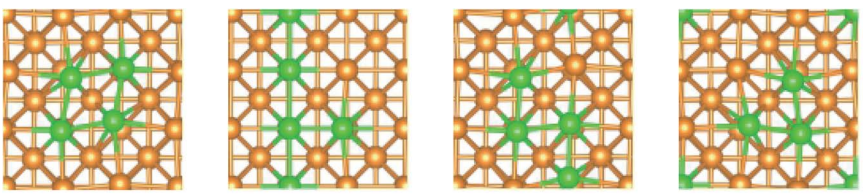

(a) M1(0 kJ/mol) (b) M2(26.19 kJ/mol) (c) M3(29.75 kJ/mol) (d) M4(56.74 kJ/mol)

Fig. 1 Top views and the relative energies for four different arrangements of four Fe atoms embedded in the toplayer of Cu(100) surface, Cu Orange Fe green.

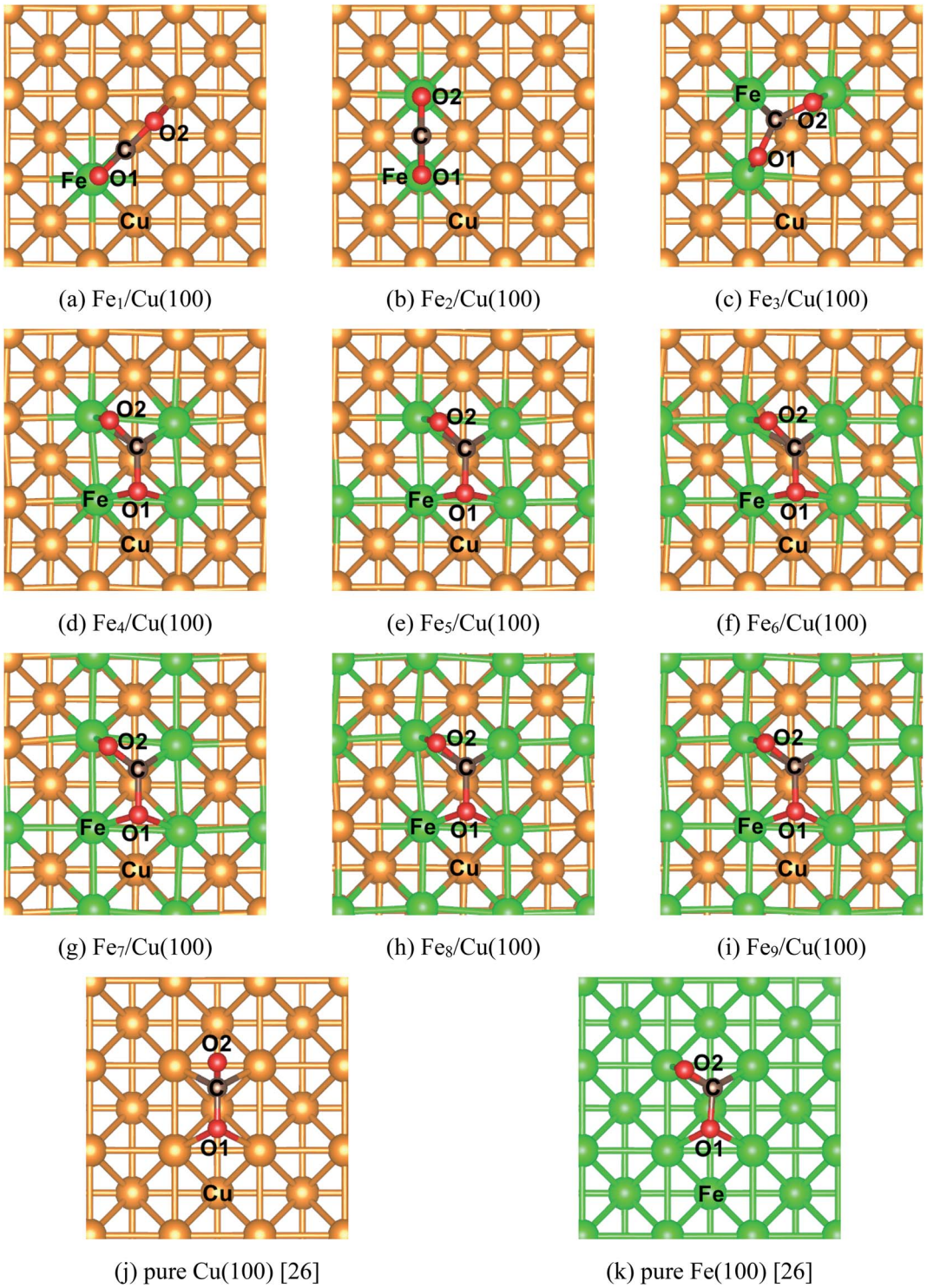

Fig. 2 Top views of the most stable configurations of CO_2 adsorbed on the different $Fe_xCu(100)$ surfaces, as well as on the pure Cu(100) and Fe(100) surfaces with fcc structure.

length was 2.014 Å (Fe_4/Cu(100)), 2.000 Å (Fe_5/Cu(100)), 1.987 Å (Fe_6/Cu(100)), 1.974 Å (Fe_7/Cu(100)), 1.961 Å (Fe_8/Cu(100)) and 1.965 Å (Fe_9/Cu(100)). Among these Fe–O2 bonds, the distance of the Fe–O2 bond for CO_2 on the Fe_4/Cu(100) was the longest, requiring the less energy barrier to decompose CO_2. The calculated adsorption energy (see Table 1) increased monotonously as an increase of the coverage for Fe atoms, suggesting that introducing Fe atoms in the pure Cu(100) surface could improve the bonding strength of CO_2 to the substrate. Compared with the adsorption energy of CO_2 on the pure Cu(100) ($E_{ads} = -72.4$ kJ mol^{-1}) and Fe fcc(100) ($E_{ads} = 139.8$ kJ mol^{-1}) surfaces,[26] the binding strength of CO_2 on the

Table 1 Some optimized bond lengths (Å), O–C–O bond angle (degrees) and the calculated adsorption energies (E_{ads}, in kJ mol^{-1}) of CO_2 molecules on pure Fe(100), Cu(100) and different Fe_x/Cu(100) bimetallic surfaces

System	d_{C-O1}[a]	d_{C-O2}	∠O–C–O	d_{Fe-C}	d_{Fe-O1}	d_{Cu-O2}	d_{Fe-O2}	E_{ads}
Fe_1/Cu(100)	1.258	1.271	134.5	1.929	2.015	2.163	—	84.5
Fe_2/Cu(100)	1.253	1.253	138.9	2.041 (×2)[b]	2.091	—	2.092	115.9
Fe_3/Cu(100)	1.296	1.295	124.4	1.939	1.969	—	1.971	135.3
Fe_4/Cu(100)	1.356	1.293	121.3	2.113/1.936	2.039/2.040	—	2.014	145.3
Fe_5/Cu(100)	1.354	1.296	121.2	2.116/1.936	2.046/2.048	—	2.000	148.6
Fe_6/Cu(100)	1.351	1.299	121.2	2.160/2.050	2.048/2.050	—	1.987	153.0
Fe_7/Cu(100)	1.362	1.296	118.5	2.115/1.938	2.047/2.013	—	1.974	147.4
Fe_8/Cu(100)	1.361	1.300	118.3	2.167/1.924	2.028/2.009	—	1.961	154.8
Fe_9/Cu(100)	1.364	1.299	118.3	2.138/1.924	2.038/2.009	—	1.965	150.8
纯 Cu(100)[c]	1.322	1.220	128.4	2.157	2.098	—	—	−72.4
纯 Fe(100)[c]	1.340	1.290	120.5	2.190/1.950	2.040/2.080	—	1.990	139.8

[a] The symbols O1 and O2 represent the two oxygen atoms of the CO_2 moiety (see Fig. 2). For the free CO_2 molecule, the optimized length of the C–O bond is 1.176 Å. [b] The number of bonds is shown in parentheses. [c] The data origin from the ref. 20.

substrate was enhanced while the coverage of Fe atoms was more than 3/9 ML.

3.2. Electronic structures of CO_2 on Fe_x/Cu(100) surfaces

3.2.1. D-Band center analysis. To interpret a variation in adsorption energy as an increase of coverage for Fe atoms, the position of the d-band center of the Fe_x/Cu(100) surface was calculated. As well-known, the d-band center model was used widely to understand the bond formation on a transition metal surface, this is, the higher the d-band center, the stronger the adsorption bond.[33] As shown in Fig. 3(a), the value of the d-band center for the Fe_x/Cu(100) surface was in the range of 2.0 to −0.7 eV and tended to increase with an increase of Fe atoms on the Cu(100) surface. Although the coverage exceeded 3/9 ML, the variation of adsorption energy was small as the increase of position of the d-band center because of the same structure of the CO_2 on Fe_x/Cu(100) surface. Furthermore, to gain a deeper understanding of the active state of the Fe_x/Cu(100) surface, the position of the d-band center for alpha (α) and beta (β) states in 3d-orbitals was extracted from the total position of the d-band center. As shown in Fig. S2† and 3(b), the trend of the variation of the d-band center for β-states orbitals was consistent with that of the total d-band center, which meant that CO_2 was adsorbed on the Fe_x/Cu(100) surface by interaction with the β-states orbitals of the doped Fe atoms. Furthermore, the calculated density of states (DOS) in Fig. 4 confirmed that, after CO_2 adsorption on Fe_x/Cu(100) surface, CO_2 tended to interact with the β-states of the substrates.

3.2.2. Bader charge analysis. As mentioned, the CO_2 on the substrate exhibited the bent structure, indicating that some electrons were transferred to CO_2 from substrate. To verify this conclusion more clearly, the charge density of CO_2 on the Fe_x/Cu(100) surface was calculated and shown in Fig. S3–S10.† Taking CO_2 on the Fe_4/Cu(100) surface as an example, Fig. 5(a) represents the charge density map of CO_2 adsorbed on the Fe_4/Cu(100) surface (the *x*-axis represents the distance from the bottom to the top of the Fe_4/Cu(100) system). Five high-density

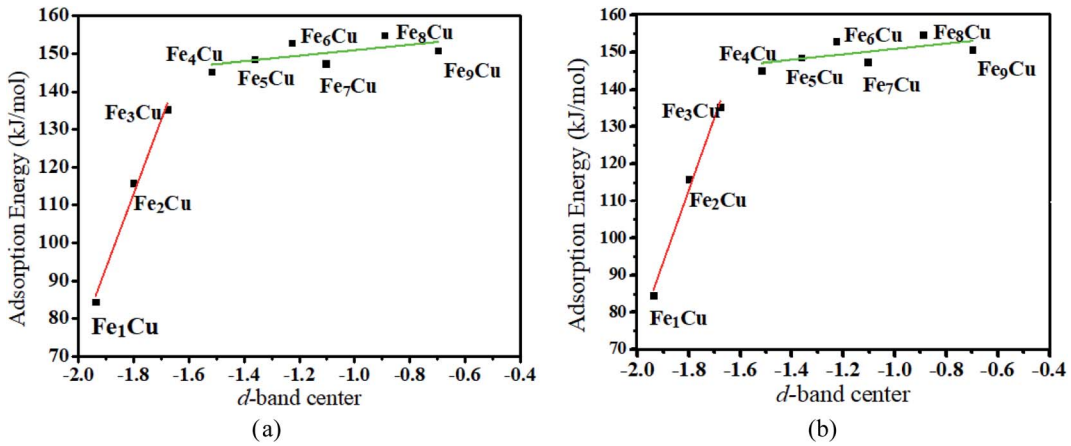

Fig. 3 Relationship between (a) the total d-band center (b) the d-band center for beta-orbitals of different Fe_x/Cu(100) surface and the adsorption energies of CO_2 molecule.

peaks in Fig. 5(a) were observed and each peak represented the charge density of one atomic layer in the Fe_4/Cu(100) surface. Furthermore, a relatively small density peak is observed at ~9.0 Å along the *x*-axis, which represented the charge density of the CO_2 moiety. It was noted that an obvious interaction between CO_2 and the Fe_4/Cu(100) surface was observed at $z = 7$–9 Å. The charge density difference map ($\Delta\rho$) in Fig. 5(b) changed from lightly positive to negative upon crossing the Fe_4/Cu(100) interface ($z = 7.0$–8.0 Å) and reached a minimum at $z = \sim 8.6$ Å. Then it changed from negative to positive in the region ($z = 8$–9 Å). This evolution indicated that the electrons flowed from the Fe_4/Cu(100) surface to the CO_2 moiety, forming the CO_2^- anions.

To quantify these charges transferred, the Bader charge analysis for all systems was calculated, as shown in Table 2. As expected, CO_2 obtained some electrons from the Fe_x/Cu(100) surfaces. In general, as the coverage increased for Fe atoms, the electrons obtained by CO_2 from the surface also increased. In particular, for the Fe_9/Cu(100) surface, the transferred electrons reached the maximum (1.17*e*). The atomic charges for C and O atoms of CO_2 moiety were also included in Table 2. It was obviously evident in Table 2 that the transferred electrons were significantly concentrated on C atom.

Fig. 6 displays the charge density difference for CO_2 moiety on Fe_x/Cu(100) surface. If the coverage was less than 4/9 ML, the π-bond between C and O1 atoms was weakened slightly, especially the Fe_1/Cu(100). Although the coverage was more than 3/9 ML, Fig. 6(d)–(i) clearly showed that the degree of activation for the π-bond was quite similar and was more larger than CO_2 on the $Fe_{1\sim3}$/Cu(100) surface.

3.2.3. Vibrational frequencies analysis. According to the Bader charge analysis, after CO_2 adsorbed on the Fe_x/Cu(100) surface, some electrons were transferred from the substrate to CO_2 moiety and concentrated on the C atom, which weakened the C–O bond and further caused a red shift of the vibrational frequency for C–O bond, especially the C–O1 bond. Table 3 present the stretching vibration frequency of C–O1 and C–O2 bonds in CO_2 moiety on each of the Fe_x/Cu(100) surface. Compared with stretching vibration frequency of a free CO_2 molecule, the stretching vibration frequency of the C–O1 and C–

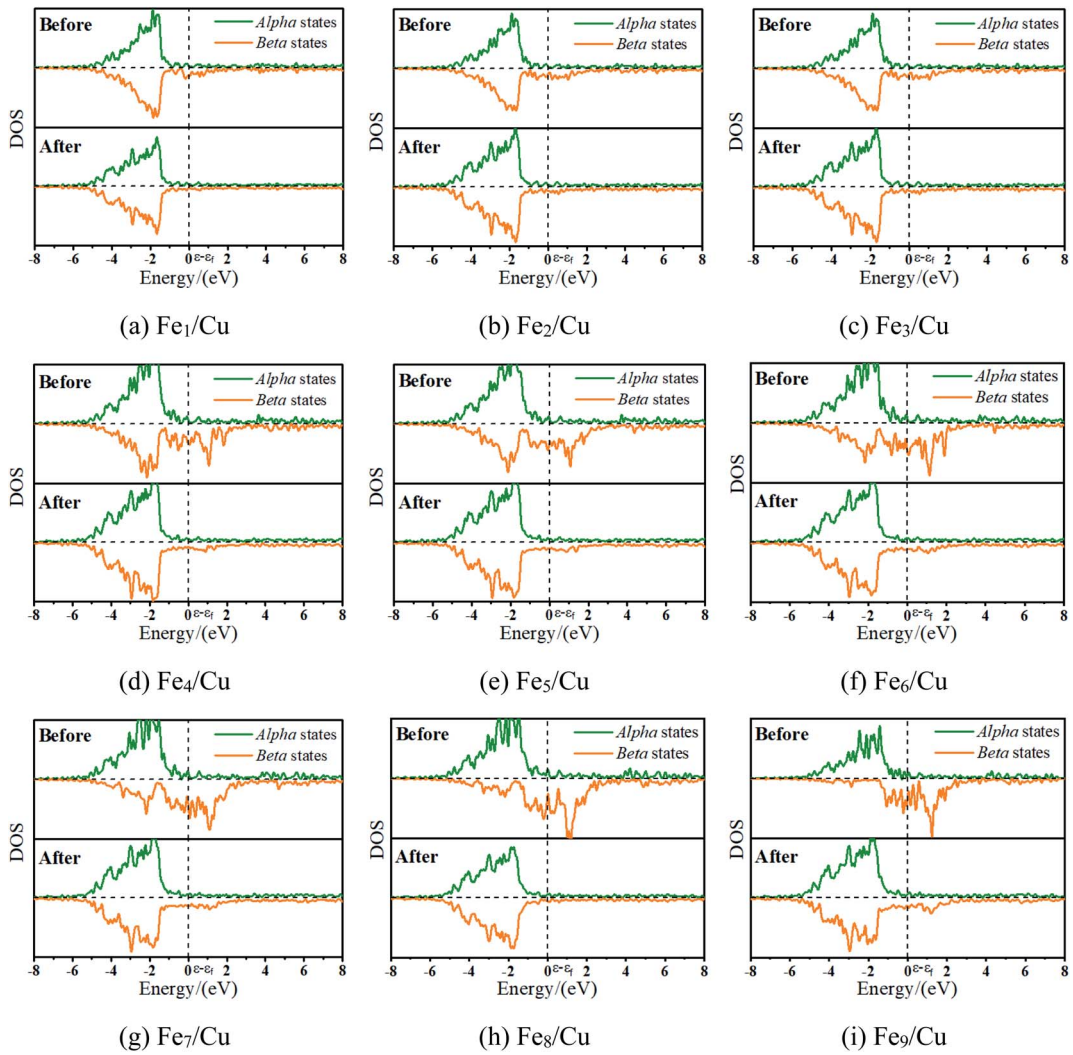

Fig. 4 The density of states for the toplayer metallic atoms in clean Fe_x/Cu(100) and CO_2/Fe_x/Cu(100) surfaces.

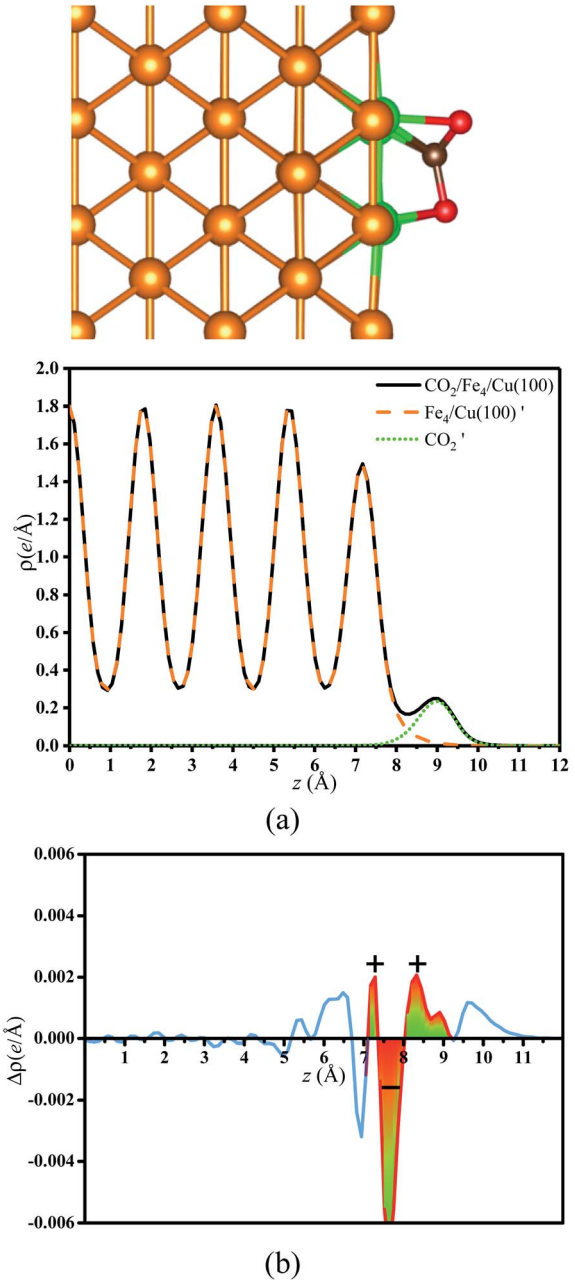

Fig. 5 (a) Charge density curves of isolated $Fe_4/Cu(10)'$ surface, CO'_2 moiety and $CO_2/Fe_4/Cu(100)$ surface. (b) Charge density difference curve of $CO_2/Fe_4/Cu(100)$ surface: $\Delta\rho(z) = \rho_{CO_2/Fe_4/Cu(100)}(z) - \rho_{CO'_2}(z) - \rho_{Fe_4/Cu(100)'}(z)$. $Fe_4/Cu(100)$ surface denotes from the $CO_2/Fe_4/Cu(100)$ system and CO'_2 is the bent CO_2 moiety of the same $CO_2/Fe_4/Cu(100)$ system.

O2 bonds was red-shifted when the CO_2 was adsorbed on the $Fe_x/Cu(100)$ surface. However, the variation of the stretching vibration frequency for C–O2 bond decreased lightly when the coverage was more than 3/9 ML. Compared with the stretching vibration frequency (1333 cm^{-1}) of the gas CO_2 molecule, the reducing value of the stretching vibration frequency for the C–O1 bond was 211 cm^{-1} ($Fe_1/Cu(100)$), 181 cm^{-1} ($Fe_2/Cu(100)$), 216 cm^{-1} ($Fe_3/Cu(100)$), 316 cm^{-1} ($Fe_4/Cu(100)$), 314 cm^{-1} ($Fe_5/Cu(100)$), 308 cm^{-1} ($Fe_6/Cu(100)$), 344 cm^{-1} ($Fe_7/Cu(100)$), 340 cm^{-1} ($Fe_8/Cu(100)$) and 354 cm^{-1} ($Fe_9/Cu(100)$), respectively. Among these frequencies, the variation of the stretching vibration frequency of the C–O1 bond adsorbed on the $Fe_9/Cu(100)$ surface reached its maximal value, which was consistent with the variation in bond length and the number of transferred charges after adsorption. Thus, the more electrons were transferred to the CO_2 molecule, the longer the C–O1 bond length was and the easier the stretching vibration frequency for the C–O1 bond was to redshift.

Table 2 Bader charges (e) of the CO_2 moiety, the carbon and oxygen atoms of different $Fe_x/Cu(100)$ surfaces and the free CO_2 molecule

	C	O1	O2	CO_2 moiety
CO_2	1.94	−0.97	−0.97	0
$Fe_1/Cu(100)$	1.29	−1.07	−0.99	−0.77
$Fe_2/Cu(100)$	1.24	−1.01	−1.01	−0.78
$Fe_3/Cu(100)$	1.14	−1.03	−1.04	−0.93
$Fe_4/Cu(100)$	0.98	−1.06	−1.04	−1.12
$Fe_5/Cu(100)$	0.90	−1.02	−1.00	−1.13
$Fe_6/Cu(100)$	0.96	−1.08	−1.02	−1.14
$Fe_7/Cu(100)$	0.92	−1.03	−1.04	−1.15
$Fe_8/Cu(100)$	0.94	−1.08	−1.02	−1.16
$Fe_9/Cu(100)$	0.94	−1.08	−1.03	−1.17
Pure Cu(100)[a]	1.47	−1.10	−1.00	−0.63
Pure Fe fcc(100)[a]	1.02	−1.12	−1.05	−1.16

[a] The data origin from ref. 20.

3.3. Decomposition of CO_2 on $Fe_x/Cu(100)$ surfaces

3.3.1. Transition state analysis. The minimum potential energy map for the decomposition of CO_2 molecules on the $Fe_x/Cu(100)$ surfaces was determined using the CI-NEB and DIMER methods and shown in Fig. 7 and S11† According to the $Fe_1/Cu(100)$ surface shown in Fig. S11(a),† the O atom bonded to three Cu atoms and one Fe atom (4-fold site), whereas the CO moiety was adsorbed between two adjacent Cu atoms. On all other $Fe_x/Cu(100)$ surfaces, the O atom was still bonded to four metal atoms to form the 4-fold site and the C atom of CO moiety was co-adsorbed to the substrate with an incline through the Fe–C adsorption bond. The reaction energy (H) of CO_2 decomposition on the $Fe_x/Cu(100)$ surface was calculated, as shown in Fig. 7 and S11.† For the $Fe_1/Cu(100)$ surface, the highest reaction energy was −4.9 kJ mol^{-1}, followed by the $Fe_3/Cu(100)$ surface (−36.1 kJ mol^{-1}) and the $Fe_2/Cu(100)$ surface (−43.1 kJ mol^{-1}). When the coverage of Fe atoms was more than 3/9 ML, the reaction energy could be significantly increased with −65.0 kJ mol^{-1} for the $Fe_4/Cu(100)$, −62.3 kJ mol^{-1} for the $Fe_5/Cu(100)$ surface, −70.7 kJ mol^{-1} for the $Fe_6/Cu(100)$ surface, −121.0 kJ mol^{-1} for the $Fe_7/Cu(100)$ surface, −122.5 kJ mol^{-1} for the $Fe_8/Cu(100)$ surface and −127.6 kJ mol^{-1} for the $Fe_9/Cu(100)$ surface. It was noteworthy that the reaction energy of the $Fe_x/Cu(100)$ surface increased with the coverage of the Fe atom increased on the Cu(100) surface, indicating that the introduced Fe atom improved the reaction energy of CO_2 decomposition. It may be reasonable

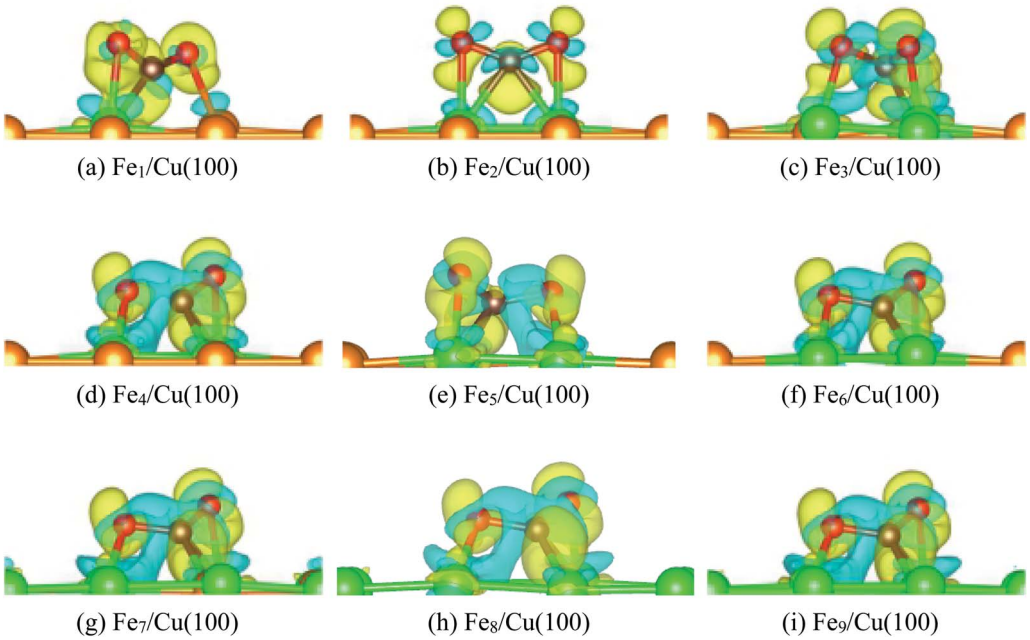

Fig. 6 Charge density difference of CO_2 on Fe_x/Cu(100) ($x = 1$–9) surface.

that, as the coverage of Fe atoms increased, the number of Fe–O bonds increased and the strength of Fe–O bond was stronger than that of Cu–O bond, thereby reaction energy was increased for CO_2 decomposition from Fe_1/Cu(100) to Fe_9/Cu(100) surfaces. From the thermodynamic point of view, the negative reaction energy indicated that the Fe_x/Cu(100) surface would be favorable to decompose CO_2 into CO, especially the Fe_9/Cu(100) surface.

The activation energy barrier (E_a) of CO_2 decomposition on the Fe_x/Cu(100) surface was determined and shown in Fig. 7 and S11.† In addition, the vibration frequencies of all transition states were calculated to ensure that the predicted TS corresponds to the first-order saddle point in the reaction path and the imaginary frequency (ν_i) was also shown in Fig. 7 and S11.† For the Fe_1/Cu(100) surface, only one TS for the C–O1 bond decomposition was discovered. The activation energy barrier (relative to the energy of the CO_2 adsorption) of CO_2 decomposed on the Fe_1/Cu(100) surface was 45.6 kJ mol^{-1}. For the Fe_2/Cu(100) and Fe_3/Cu(100) surfaces, the activation energy barrier increased to 59.9 kJ mol^{-1} and 63.7 kJ mol^{-1} compared with the Fe_1/Cu(100) surface, respectively. When the coverage reached 4/9 ML, the activation energy barrier reached the minimum value (32.8 kJ mol^{-1}). The transition state of CO_2 decomposition on the Fe_x/Cu(100) surface was extremely similar to the CO_2 on the Fe_4/Cu(100) surface when the coverage was greater than 4/9 ML. The corresponding activation energy barrier from the Fe_5/Cu(100) to Fe_9/Cu(100) systems was 35.4 kJ mol^{-1}, 39.7 kJ mol^{-1}, 34.7 kJ mol^{-1}, 40.2 kJ mol^{-1} and 35.0 kJ mol^{-1}, respectively. The results showed that the activation energy barrier of all systems exhibited an inverted "S" shape, which was

Table 3 The stretching vibration of the C–O1 and C–O2 bonds in CO_2 moiety on Fe_x/Cu(100) surface and free CO_2

System	ν_{C-O1}/cm^{-1}	ν_{C-O2}/cm^{-1}
Free CO_2[a]	1333	1333
Fe_1/Cu(100)	1122	1610
Fe_2/Cu(100)	1152	1152
Fe_3/Cu(100)	1117	1117
Fe_4/Cu(100)	1017	1305
Fe_5/Cu(100)	1019	1296
Fe_6/Cu(100)	1025	1283
Fe_7/Cu(100)	989	1279
Fe_8/Cu(100)	993	1258
Fe_9/Cu(100)	979	1261

[a] The data origin from NIST database: https://webbook.nist.gov/chemistry.

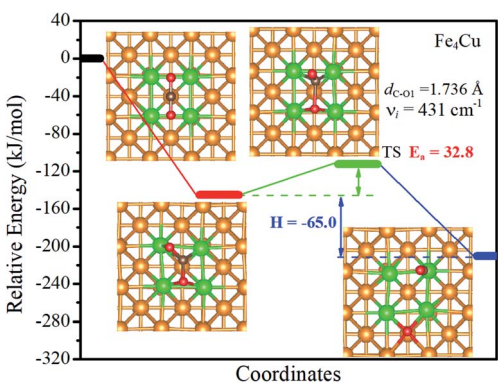

Fig. 7 Calculated reaction paths of CO_2 dissociation on the Fe_4/Cu(100) surface. The zero of energy is set to the total energy of the isolated surface and CO_2 molecule in the gas phase.

consistent with the variation in the distance between Fe and O2 atoms, that is, the shorter the distance of the Fe–O2 adsorption bond, the larger the activation energy barrier. For instance, the length (2.014 Å) of the Fe–O2 adsorption bond formed on the Fe_4/Cu(100) surface was the largest among the Fe_x/Cu(100) system, which indicated that the O2 atom may need to consume less additional energy to "escape" out of the substrate. Therefore the activation energy barrier of CO_2 decomposition on the Fe_4/Cu(100) surface was minimal. In addition, Fe dopant introduced on the Cu(100) surface significantly reduced the activation energy barrier of CO_2 decomposition compared with the barrier of CO_2 on the pure Cu(100) surface with the barrier of 92.9 kJ mol^{-1} and the Fe(100) surface with the barrier of 113.4 kJ mol^{-1}, especially the Fe_4/Cu(100) system.[26] Compared to CO_2 on the Co_4/Cu(100) surface with the barrier of 18.7 kJ mol^{-1},[33] the activation energy barrier for CO_2 on the Fe_x/Cu(100) is more than 14.1 kJ mol^{-1}. The main reason is that bond strength of Fe–O (in diatomic molecules: 390.4 kJ mol^{-1}) is stronger than that of Co–O (in diatomic molecules: 384.5 kJ mol^{-1}), which led to be the extra barrier formed by Fe–O bond to overcome.

Moreover, the reaction energy barrier ($\Delta E_a = E_{TS} - E_{Slab} - E_{CO_2}$) and the total reaction energy ($\Delta E = E_{ads} + H$) followed a linear relationship for the C–O bond scission and the BEP relationship was established: $\Delta E_a = 0.4\Delta E - 2.5$ (kJ mol^{-1}) (see Fig. 8). This BEP relationship played an important role in estimating the reaction barrier of the C–O bond scission on other metal surfaces. Furthermore, the results in Fig. 3 showed an increasing trend as the number of Fe-dopants increased. It was worth noting that although the Fe_4/Cu(100) surface did not have the lowest reaction energy barrier and total reaction energy, the Fe_4/Cu(100) surface had the lowest activation energy barrier for CO_2 decomposition, which facilitated the decomposition of CO_2.

3.3.2. Micro kinetics analysis. To further explore the mechanism of CO_2 decomposition on the Fe_x/Cu(100) surfaces from the perspective of dynamics, a microkinetic analysis based on the DFT studies was employed on the most favorable path of CO_2 decomposition.[62,63] In the microkinetic model, the temperatures ranging from 250 to 1000 K was adopted to investigate its impact.

The zero point energy, entropy and enthalpy corrections for the activation energy barrier (E_a) were considered to accurately describe the reaction at high temperatures (from 250 to 1000 K) in this section. The obtained results were presented in Tables S2–S19.† The forward and reverse rate constants of the elementary reaction steps for CO_2 decomposition on the Fe_x/Cu(100) surfaces at temperature ranging from 250 to 1000 K were displayed in Fig. 9. The Fig. 9 showed that the forward rate constants and inverse rate constants for the CO_2 decomposition on the Fe_x/Cu(100) surfaces increased as the temperature increased. At the same temperature, the rate constants for CO_2 dissociation increased with an increase in the coverage of dopant Fe atom, indicating that the doped Fe significantly improved the rate constants. Moreover, it was further noting that the both forward rate constants and inverse rate constants for CO_2 decomposition was not only increased as the increase of temperature, but the forward rate constants in all Fe_x/Cu(100) surface were much larger than the inverse rate constants. In addition, the equilibrium constants ($K = k_+/k_-$) of CO_2 decomposition on the Fe_x/Cu(100) surfaces were also considered as a critical parameter. As shown in Fig. 10 and in Tables S11–S19,† the K decreased as the temperature increased, which meant that the increase in the inverse rate constants was greater than the positive rate constants as the temperature increased. The nine curves for K (equilibrium constants) were divided into four groups, *i.e.* G1 (Fe_1/Cu system), G2 (Fe_2/Cu and Fe_3/Cu systems), G3 (Fe_4/Cu, Fe_5/Cu and Fe_6/Cu systems), G4 (Fe_7/Cu, Fe_8/Cu and Fe_9/Cu systems). In each group the equilibrium constants were close to each other, which was agreement with the variation in the BEP relationship. According to the K, the order of the four group was G4 > G3 > G2 > G1 at the same temperature. Thus, the doped Fe atom was favorable to be activation and decomposition of CO_2 molecule and the K of CO_2 decomposition increased as the coverage of the Fe atom increased. Moreover, although increasing temperature was favorable to the increases of the forward rate constants and invers rate constants, it was unfavorable to the increase of the equilibrium constants. From

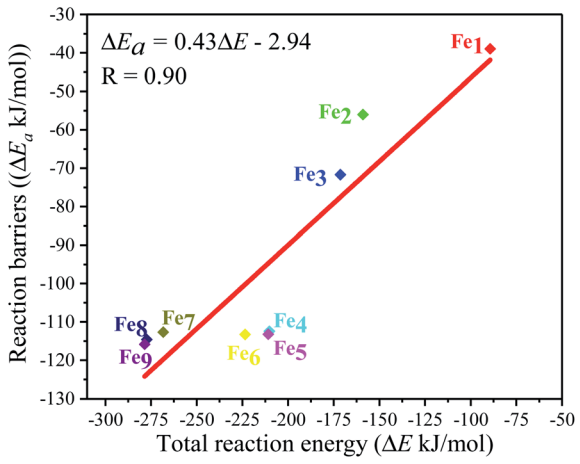

Fig. 8 Brønsted–Evans–Polanyi (BEP) relationship for the C–O1 bond scission of CO_2 on the Fe_x/Cu(100) (x = 1–9) surfaces.

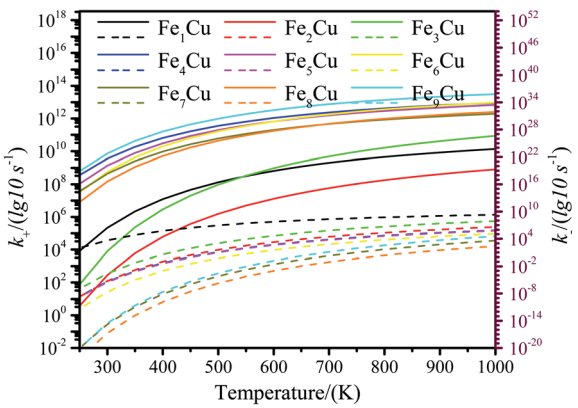

Fig. 9 The forward and reverse rate constants for CO_2 decomposition on the Fe_x/Cu(100) surfaces at temperature from 250 K to 1000 K. (The solid line represents the positive equilibrium constants and the dashed line is the inverse equilibrium constants).

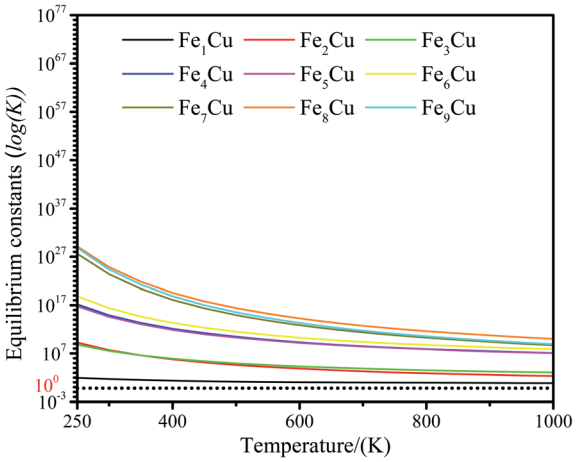

Fig. 10 Equilibrium constants for CO_2 decomposition on the Fe_x/Cu(100) surface at temperature from 250 to 1000 K.

the perspective of dynamics, this results indicated that the lower the temperature for CO_2 decomposition, the more favorable the decomposition of CO_2 on the Fe_x/Cu(100) surface.

3.3.3. Effects of partial pressure of CO_2. Fig. 11 illustrated the impact of partial pressure of CO_2 towards the decomposition of CO_2. The results in Fig. 11(a) showed that the decomposition of CO_2 into CO at partial pressure from 0 to 10 atm was not obviously observed when the temperature was less than 300 K. While the concentration of CO reached 50% at the partial pressure of 0.5 atm when the temperature is higher than or equal to 300 K. To further explore the decomposition of CO_2 at the low partial pressure of CO_2, the partial pressure of CO_2 from 0 atom to 0.01 atm was studied and the results were shown in Fig. 11(b). It was seen in Fig. 11(b) that when the temperature is below 300 K, the decomposition reaction of CO_2 was not observed at the partial pressure from 0 atm to 0.01 atm; The relative concentration of CO increased with the partial pressure of CO_2 increased when the temperature was at 350 K; if the temperature was greater than 350 K, the concentration of CO reached 49% at the partial pressure of 0.0003 atm (in general, the partial pressure of CO_2 in the atmosphere is less than 0.03%). Therefore, when the temperature was greater than 350 K, CO_2 could be decomposed into CO on Fe_4/Cu(100) surface under the normal partial pressure of CO_2 in the atmosphere.

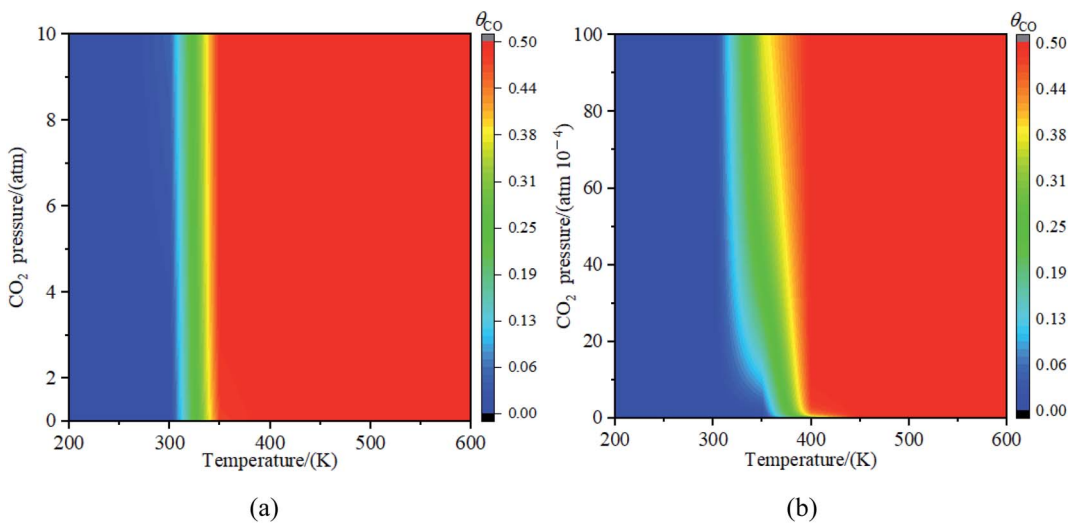

Fig. 11 The concentration of CO on Fe_4/Cu(100) surface with the partial pressure for CO_2 (a) from 0 to 10 atm and (b) from 0 to 0.01 atm.

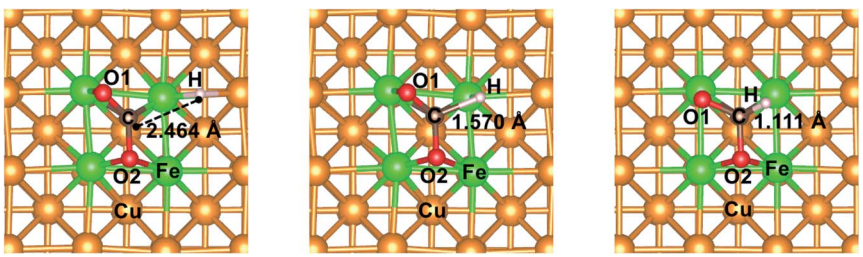

Fig. 12 The structures of initial structure (IS), translation structure (TS) and final structure (FS) for CO_2 hydrogenation to HCOO* on the Fe_4/Cu(100) surface.

3.4. Hydrogenation of CO_2 on Fe_4/Cu(100) surface

The mechanism of CO_2 hydrogenation on the Fe_4/Cu(100) surface was also examined in this section. There were three reaction pathways for CO_2 hydrogenation: the C atom was attacked by H atom and the O1 and O2 atom was attacked, respectively. However, our previous works reveal that the hydrogenation of the C atom in CO_2 moiety is more favorable than that of the O atom.[16,33,34] Thus, the C atom hydrogenation was considered as an important reaction pathway while CO_2 moiety was dissociated. The initial structure (IS), translation structure (TS) and finally structure (FS) was presented in Fig. 12. In Fig. 12, the distance between C and H atoms was changed from 2.464 Å in the IS to 1.570 Å in the TS, and then to 1.111 Å in the FS. The translation structure had been confirmed by the single imaginary frequency with 686 cm^{-1}. It was worth noted that the calculated activation energy barrier of CO_2 hydrogenation to HCOO* was 31.8 kJ mol^{-1}, which was less 1.0 kJ mol^{-1} than that of decomposition for CO_2 on the Fe_4/Cu(100) surface. Such the small difference suggests that CO_2 hydrogenation could also be performed during the CO_2 decomposition. To understand the relationship between hydrogenation and dissociation of CO_2, the FPMD was carried to the system with CO_2 and H co-adsorption on Fe_4/Cu(100) surface at temperature from 250 to 450 K. The radial distribution function of C–O suggests that the broad peak was observed from 2.5 to 3.5 Å in Fig. S15(a)† and it was not found for the peak of C–H in Fig. S15(b)† and O–H in Fig. S15(c)† from 1.0 to 1.5 Å at 400 K. This means that CO_2 would rather decompose than hydrogenate at 400 K.

4. Conclusions

The adsorption, activation and reduction of CO_2 molecule on the Fe_x/Cu(100) (x = 1–9) had been investigated by the density functional theory based on the first principle. The results indicated that the introduction of dopant Fe atom could enhance the adsorption and activation of CO_2 molecule on the Cu(100) surface. The most stable structure for CO_2 on the Fe_x/Cu(100) surface was sensitive to the coverage of the Fe dopant. The electronic structural analysis, including d-band center, Bader charge, vibrational frequencies, showed that CO_2 molecule interacted with the β-state orbitals of the Fe_x/Cu(100) surface. After CO_2 adsorption, some electrons were transferred from substrate to CO_2 moiety and the electrons transferred to CO_2 moiety increased with the coverage of Fe atoms increased, leading to formation of CO_2^- anion. Additionally, the mechanism of CO_2 moiety decomposition on Fe_x/Cu(100) surfaces had been studied in detail. The results indicated that the activation energy barrier (E_a = 32.8 kJ mol^{-1}) of CO_2 decomposition on Fe_4/Cu(100) was the smallest among the Fe_x/Cu(100) surfaces. The major reason was that, if coverage was more than 4/9 ML, the extra formed Fe–O2 bond played an handle role for CO_2 decomposition. From the viewer of kinetic, the rate constants of CO_2 on Fe_4/Cu(100) surface were close to that of the Fe_9/Cu(100) surface and the equilibrium constants analysis revealed that the servers of the equilibrium constants were divided into the four group, and the order of the four groups was G1 (Fe_1/Cu) > G2 (Fe_2/Cu and Fe_3/Cu) > G3 (Fe_4/Cu, Fe_5/Cu and Fe_6/Cu) > G4 (Fe_7/Cu, Fe_8/Cu and Fe_9/Cu). Furthermore, our results confirmed that the lower the temperature, the more favorable it was to decompose the CO_2 molecule into CO. When the simulated temperature was in range from 350 K and 450 K, the decomposition of C–O1 bond in CO_2 moiety was only observed. The results of partial pressure for CO_2 revealed that when the temperature was in range from 350 K to 450 K, the concentrate of CO on the Fe_4/Cu(100) surface reached 49% under the partial pressure of 3×10^{-4} atm. Lastly, the mechanism of CO_2 hydrogenation on the Fe_4/Cu(100) surface was also investigated. The activation energy barrier of 31.8 kJ mol^{-1} was slightly less than that of CO_2 decomposition. However, the results of the FPMD analysis revealed that CO_2 was decomposed to form CO*, instead of hydrogenated. Our results provide insight into the mechanism for CO_2 decomposition and hydrogenation on bimetallic surfaces from the perspective of thermodynamics and kinetics, which was important for the design and optimization of novel Cu-based bimetallic catalysts.

Conflicts of interest

The authors declare that they have no known competing financial interests or personal relationships that could have appeared to influence the work reported in this paper.

Acknowledgements

The author is grateful to Prof. Yongfan Zhang who contributes the VASP Package and provides lots of help for this research. Financial support for this research was provided by National Natural Science Foundation of China (grant no. 21773030) and Natural Science Foundation of Jiangxi Provincial Department of Education (grant no. GJJ170304).

References

1 S. Kar, R. Sen, A. Goeppert and G. S. Prakash, *J. Am. Chem. Soc.*, 2018, **140**, 1580–1583.
2 G. Gao, Y. Jiao, E. R. Waclawik and A. Du, *J. Am. Chem. Soc.*, 2016, **138**, 6292–6297.
3 D. A. Torelli, S. A. Francis, J. C. Crompton, A. Javier, J. R. Thompson, B. S. Brunschwig, M. P. Soriaga and N. S. Lewis, *ACS Catal.*, 2016, **6**, 2100–2104.
4 E. R. Cave, C. Shi, K. P. Kuhl, T. Hatsukade, D. N. Abram, C. Hahn, K. Chan and T. F. Jaramillo, *ACS Catal.*, 2018, **8**, 3035–3040.
5 I. Ledezma-Yanez, E. P. Gallent, M. T. Koper and F. Calle-Vallejo, *Catal. Today*, 2016, **262**, 90–94.
6 H. Kumagai, T. Nishikawa, H. Koizumi, T. Yatsu, G. Sahara, Y. Yamazaki, Y. Tamaki and O. Ishitani, *Chem. Sci.*, 2019, **10**, 1597–1606.
7 F. Pan, B. Li, W. Deng, Z. Du, Y. Gang, G. Wang and Y. Li, *Appl. Catal., B*, 2019, **252**, 240–249.
8 Y. Pi, J. Guo, Q. Shao and X. Huang, *Nano Energy*, 2019, **62**, 861–868.

9 X. Li, W. Bi, L. Zhang, S. Tao, W. Chu, Q. Zhang, Y. Luo, C. Wu and Y. Xie, *Adv. Mater.*, 2016, **28**, 2427–2431.
10 E.-X. Chen, M. Qiu, Y.-F. Zhang, Y.-S. Zhu, L.-Y. Liu, Y.-Y. Sun, X. Bu, J. Zhang and Q. Lin, *Adv. Mater.*, 2018, **30**, 1704388.
11 S. Remiro-Buenamañana and H. García, *ChemCatChem*, 2018, **11**, 342–356.
12 Y. Hartadi, D. Widmann and R. J. Behm, *J. Catal.*, 2016, **333**, 238–250.
13 M. Qiu, H. Tao, R. Li, Y. Li, X. Huang, W. Chen, W. Su and Y. Zhang, *J. Chem. Phys.*, 2016, **145**, 134701.
14 S. Kuld, M. Thorhauge, H. Falsig, C. F. Elkjær, S. Helveg, I. Chorkendorff and J. Sehested, *Science*, 2016, **352**, 969–974.
15 P. Gao, S. Li, X. Bu, S. Dang, Z. Liu, H. Wang, L. Zhong, M. Qiu, C. Yang, J. Cai, W. Wei and Y. Sun, *Nat. Chem.*, 2017, **9**, 1019–1024.
16 T. Wagner, U. Ermler and S. Shima, *Science*, 2016, **354**, 114–117.
17 Y. Zheng, W. Q. Zhang, Y. F. Li, J. Chen, B. Yu, J. C. Wang, L. Zhang and J. J. Zhang, *Nano Energy*, 2017, **40**, 512–539.
18 G. X. Zhao, X. B. Huang, X. X. Wang and X. K. Wang, *J. Mater. Chem. A*, 2017, **5**, 21625–21649.
19 A. Víctor, S. González, F. Illas and J. L. Fierro, *Chem. Phys. Lett.*, 2008, **454**, 262–268.
20 S.-G. Wang, D.-B. Cao, Y.-W. Li, J. Wang and H. Jiao, *J. Phys. Chem. B*, 2005, **109**, 18956–18963.
21 A. Farjamnia and B. Jackson, *J. Chem. Phys.*, 2017, **146**, 074704.
22 P. Rasmussen, P. Taylor and I. Chorkendorff, *Surf. Sci.*, 1992, **269**, 352–359.
23 H.-J. Freund and M. W. Roberts, *Surf. Sci. Rep.*, 1996, **25**, 225–273.
24 X. Ding, V. Pagan, M. Peressi and F. Ancilotto, *Mater. Sci. Eng., C*, 2007, **27**, 1355–1359.
25 V.-A. Glezakou, L. X. Dang and B. P. McGrail, *J. Phys. Chem. C*, 2009, **113**, 3691–3696.
26 C. Liu, T. R. Cundari and A. K. Wilson, *J. Phys. Chem. C*, 2012, **116**, 5681–5688.
27 R. Ferrando, J. Jellinek and R. L. Johnston, *Chem. Rev.*, 2008, **108**, 845–910.
28 B. Steinhauer, M. R. Kasireddy, J. Radnik and A. Martin, *Appl. Catal., A*, 2009, **366**, 333–341.
29 J. Nerlov and I. Chorkendorff, *J. Catal.*, 1999, **181**, 271–279.
30 J. Nerlov, S. Sckerl, J. Wambach and I. Chorkendorff, *Appl. Catal., A*, 2000, **191**, 97–109.
31 J. Nerlov and I. Chorkendorff, *Catal. Lett.*, 1998, **54**, 171–176.
32 Y. Yang, M. G. White and P. Liu, *J. Phys. Chem. C*, 2011, **116**, 248–256.
33 M. Qiu, H. Tao, Y. Li, Y. Li, K. Ding, X. Huang, W. Chen and Y. Zhang, *Appl. Surf. Sci.*, 2018, **427**, 837–847.
34 M. Qiu, Z. Fang, Y. Li, J. Zhu, X. Huang, K. Ding, W. Chen and Y. Zhang, *Appl. Surf. Sci.*, 2015, **353**, 902–912.
35 X. Nie, H. Wang, Z. Liang, Z. Yu, J. Zhang, M. J. Janik, X. Guo and C. Song, *J. CO2 Util.*, 2019, **29**, 179–195.
36 X. Nie, H. Wang, M. J. Janik, X. Guo and C. Song, *J. Phys. Chem. C*, 2016, **120**, 9364–9373.
37 O. Kurnosikov, J. T. Kohlhepp and W. J. M. de Jonge, *Europhys. Lett.*, 2003, **64**, 77–83.
38 S. V. Kolesnikov, A. L. Klavsyuk and A. M. Saletsky, *J. Exp. Theor. Phys.*, 2015, **121**, 616–622.
39 G. Kresse and J. Hafner, *Phys. Rev. B: Condens. Matter Mater. Phys.*, 1993, **48**, 13115–13118.
40 G. Kresse and J. Hafner, *Phys. Rev. B: Condens. Matter Mater. Phys.*, 1993, **47**, 558–561.
41 G. Kresse and J. Hafner, *Phys. Rev. B: Condens. Matter Mater. Phys.*, 1994, **49**, 14251–14269.
42 G. Kresse and D. Joubert, *Phys. Rev. B: Condens. Matter Mater. Phys.*, 1999, **59**, 1758–1775.
43 P. E. Blöchl, *Phys. Rev. B: Condens. Matter Mater. Phys.*, 1994, **50**, 17953–17979.
44 J. Hafner, *J. Comput. Chem.*, 2008, **29**, 2044–2078.
45 J. P. Perdew, K. Burke and M. Ernzerhof, *Phys. Rev. Lett.*, 1996, **77**, 3865–3868.
46 S. Grimme, *J. Comput. Chem.*, 2006, **27**, 1787–1799.
47 J. P. Ramalho, J. R. Gomes and F. Illas, *RSC Adv.*, 2013, **3**, 13085–13100.
48 H. J. Monkhorst and J. D. Pack, *Phys. Rev. B: Solid State*, 1976, **13**, 5188–5192.
49 D. Sheppard, P. Xiao, W. Chemelewski, D. D. Johnson and G. Henkelman, *J. Chem. Phys.*, 2012, **136**, 074103.
50 D. Sheppard, R. Terrell and G. Henkelman, *J. Chem. Phys.*, 2008, **128**, 134106.
51 G. Henkelman and H. Jónsson, *J. Chem. Phys.*, 1999, **111**, 7010–7022.
52 R. Olsen, G. Kroes, G. Henkelman, A. Arnaldsson and H. Jónsson, *J. Chem. Phys.*, 2004, **121**, 9776–9792.
53 G. Henkelman, A. Arnaldsson and H. Jónsson, *Comput. Mater. Sci.*, 2006, **36**, 354–360.
54 E. Sanville, S. D. Kenny, R. Smith and G. Henkelman, *J. Comput. Chem.*, 2007, **28**, 899–908.
55 W. Tang, E. Sanville and G. Henkelman, *J. Phys.: Condens. Matter*, 2009, **21**, 084204.
56 H. Eyring, *J. Chem. Phys.*, 1935, **3**, 107–115.
57 J. K. Nørskov, F. Studt, F. Abild-Pedersen and T. Bligaard, *Fundamental Concepts in Heterogeneous Catalysis*, Wiley, Hoboken, 2014, vol. 4, pp. 47–67.
58 K. J. Laidler, *Chemical Kinetics*, HarperCollins, New York, 3rd edn, 1987, vol. 4, pp. 81–129.
59 A. Bukoski, H. Abbott and I. Harrison, *J. Chem. Phys.*, 2005, **123**, 094707.
60 K. Li, C. Yin, Y. Zheng, F. He, Y. Wang, M. Jiao, H. Tang and Z. Wu, *J. Phys. Chem. C*, 2016, **120**, 23030–23043.
61 P. Liu and J. A. Rodriguez, *J. Chem. Phys.*, 2007, **126**, 164705.
62 G. Novell-Leruth, J. M. Ricart and J. Pérez-Ramírez, *J. Phys. Chem. C*, 2008, **112**, 13554–13562.
63 C.-Z. He, H. Wang, L.-Y. Huai and J.-Y. Liu, *J. Phys. Chem. C*, 2012, **116**, 24035–24045.

